CHEMISTRY OF MATERIALS
Cite This: Chem. Mater. 2019, 31, 3201−3210
Article
pubs.acs.org/cm

Magnetic Photoluminescent Nanoplatform Built from Large-Pore Mesoporous Silica

Fan Yang,[†] Artiom Skripka,[†] Maryam Sadat Tabatabaei,[‡] Sung Hwa Hong,[§] Fuqiang Ren,[†] Yue Huang,[†] Jung Kwon Oh,[§] Sylvain Martel,[‡] Xinyu Liu,[∥] Fiorenzo Vetrone,*[,†] and Dongling Ma*[,†]

[†]Institut National de la Recherche Scientifique, Centre Énergie, Matériaux et Télécommunications, Université du Québec, 1650 Boul. Lionel-Boulet, Varennes, Quebec J3X 1S2, Canada

[‡]NanoRobotics Laboratory, Department of Computer and Software Engineering, Institute of Biomedical Engineering, Polytechnique Montréal, Montreal, Quebec H3T 1J4, Canada

[§]Department of Chemistry and Biochemistry, Concordia University, Montreal, Quebec H4B 1R6, Canada

[∥]Department of Mechanical and Industrial Engineering, University of Toronto, 5 King's College Road, Toronto, Ontario M5S 3G8, Canada

Supporting Information

ABSTRACT: Integrating multiple components to realize cancer diagnosis and therapy in a single theranostic nanoplatform has drawn considerable attention. Herein, a multifunctional theranostic nanoplatform ($mSiO_2$@PbS/CdS-Fe_3O_4) was successfully fabricated by carefully designing thiol-modified large-pore mesoporous silica nanospheres ($mSiO_2$), followed by coordination-driven embedding of Fe_3O_4 nanoparticles (NPs) and PbS/CdS quantum dots (QDs) inside. The excellent feature of near-infrared (NIR) excitation and NIR emission of PbS/CdS QDs enables deep-tissue photoluminescence imaging, which was demonstrated ex vivo with tissue as thick as 14 mm. Meanwhile, owing to the presence of superparamagnetic Fe_3O_4 NPs, $mSiO_2$@PbS/CdS-Fe_3O_4 can be rapidly confined under an external magnetic field (MF), and exhibit a significantly high T_2 relaxivity in T_2-weighted magnetic resonance (MR) images in vivo. When $mSiO_2$@PbS/CdS-Fe_3O_4 was exposed to external physical stimuli of MF and/or NIR laser, they produced strong local heating through magnetothermal/photothermal effects. Owing to the unique mesoporous structure of $mSiO_2$@PbS/CdS-Fe_3O_4, doxorubicin (DOX) was readily loaded into them and the drug-release profile was subsequently evaluated under multistimuli (pH/MF/NIR). The release of DOX was significantly enhanced at lower pH, and higher temperatures caused by magnetothermal/photothermal effects. Our results pave the road toward developing a highly powerful nanoplatform for bimodal imaging (NIR deep-tissue photoluminescence and MR imaging), and simultaneously for integrating synergistic treatment capabilities of hyperthermia and pH/MF/NIR-responsive drug release.

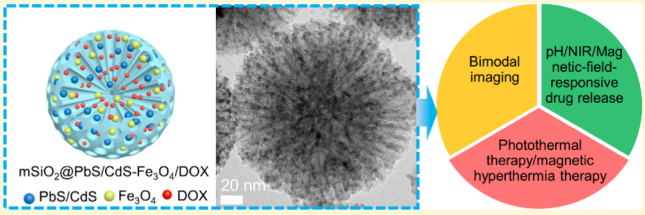

INTRODUCTION

Over the last few decades, various imaging techniques have been developed to study dynamic physiological changes in biological environments, especially for early cancer diagnosis. Magnetic resonance (MR) imaging, one of the most advanced imaging techniques, has become a staple in the clinic and is extensively applied for cancer diagnosis.[1] However, retrieving detailed subcellular information from MR imaging is difficult due to the limited spatial resolution and low contrast agent sensitivity.[2] Photoluminescence imaging, on the other hand, can potentially overcome these issues due to its high sensitivity at the subcellular level, which also has an additional advantage of relatively low cost of related imaging facilities. The combination of both, MR and photoluminescence imaging, into a single bimodal imaging platform is thus highly desired in the fight against cancer because it integrates acquisition of macroscopic and subcellular information, in turn increasing the reliability and accuracy of diagnosis. Motivated by the unprecedented efficacy of cancer diagnosis, studies that combine MR and photoluminescence imaging probes have been emerging gradually.[1,3−9] Nonetheless, among these previous studies, most of them focused on the use of visible-emitting organic dyes, upconverting nanoparticles (NPs) and quantum dots (QDs), which suffer from limited tissue penetration and whose signal can be also obscured by tissue autofluorescence in the visible range.[2−4,8−12] To solve this problem, an ideal photoluminescent component, with its absorption and emission wavelengths both located in the so-called biological windows with high optical transparency in the near-infrared (NIR) range (NIR-I: 700−950 nm; NIR-II:

Received: January 4, 2019
Revised: April 22, 2019
Published: April 24, 2019

DOI: 10.1021/acs.chemmater.9b00028
Chem. Mater. 2019, 31, 3201−3210

Scheme 1. Schematic of Fe_3O_4- and PbS/CdS-Loaded Large-Pore $mSiO_2$ ($mSiO_2$@PbS/CdS-Fe_3O_4) Nanospheres for Application in Bimodal (NIR Photoluminescence and MR) Imaging, PTT/MHT, and Simultaneous pH/NIR/MF Multiresponsive Drug Release

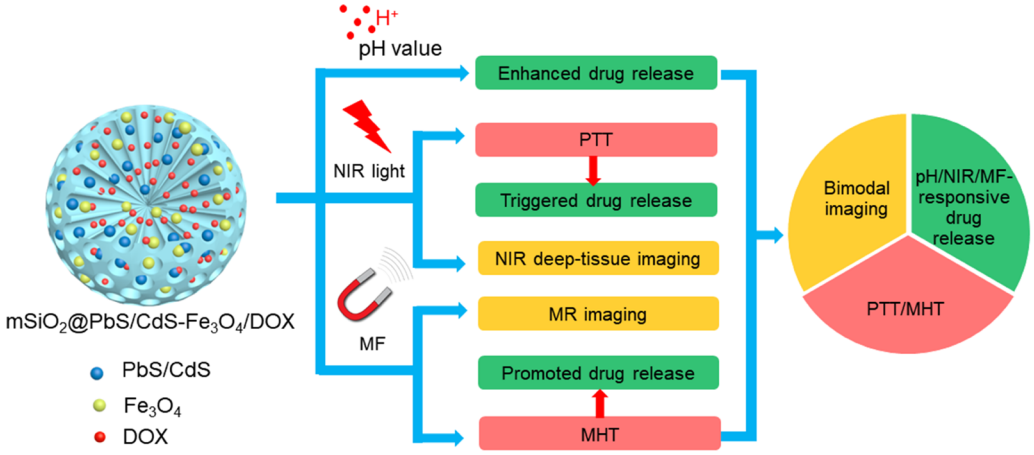

1000−1350 nm), should be specifically developed.[13,14] With the introduction of NIR-operable emitters, the bimodal imaging probe can efficiently circumvent absorption and scattering of both incident and emitted photons by endogenous tissue constituents, thus achieving deep-tissue penetrated photoluminescence imaging with a high signal-to-noise ratio.[15] Therefore, it is highly desirable to engineer new multifunctional (superparamagnetic and photoluminescent) NPs with integrated MR and NIR optical imaging for in vivo deep-tissue bimodal diagnostics.

Once the early diagnosis of cancer has been established, the survival rate for cancer can be largely increased if appropriate therapeutic strategies are timely implemented. Designing external stimulus-responsive nanoplatforms for remotely controlled cancer treatment has aroused widespread interest, as a means to potentially avoid drug overdose and reduce side effects.[16] To date, a variety of external physical stimuli, such as light, pH, temperature, and magnetic field (MF), have been used to trigger/control functional NPs-based cancer therapy.[17−20] Among these, magnetic hyperthermia therapy (MHT) using superparamagnetic NPs has been translated into the commercial clinical setting for the treatment of cancers.[21] Meanwhile, the NIR light-stimulated photothermal therapy (PTT) has become one of the research focuses rapidly approaching the clinical setting, owing to its easy operation, noninvasiveness, high specificity, and reasonable penetration.[19] Besides using heat to directly kill the cancer cells in both MHT and PTT, the thermal effect can be used to trigger the release of therapeutic drugs highly locally at specific tumor sites, thus providing a synergistically improved therapeutic efficiency compared to a single mode of MHT/PTT. A number of studies based on gold NPs, carbon nanotubes, graphene oxide, and iron oxide hybrid NPs for MHT/PTT and multiresponsive drug release have been reported.[21−24] Nonetheless, there are few research studies integrating bimodal imaging (not to mention NIR imaging), MHT/PTT, and multiresponsive drug release into one nanoplatform, which can result in a largely enhanced theranostic potential allowing for the simultaneous diagnosis and treatment of the disease.[25]

Mesoporous silica ($mSiO_2$) NPs are extensively investigated in the application of drug delivery as an alternative to traditional organic emulsions/liposomes because they generally possess a rigid mesostructured framework, high stability against various temperatures, and ease of surface modification for linking drug molecules.[16,26,27] Unfortunately, $mSiO_2$ NPs prepared by employing cetyltrimethylammonium bromide or other alkylammonium surfactants as a template usually show small pore size (<2 nm), which greatly hinders their use for encapsulation of macromolecular drugs (>2 nm) and functional NPs (iron oxide, gold, QDs, etc.).[28] Therefore, it is of paramount importance to fabricate uniform $mSiO_2$ with large pore size (>5 nm) for in vivo biomedical applications. Very recently, Zhao and co-workers have reported a novel type of three-dimensional dendritic biodegradable $mSiO_2$ nanospheres using a biphase stratification approach.[27] The average pore size of $mSiO_2$ nanospheres could be adjusted to 13 nm by adopting appropriate experimental reaction parameters. Owing to their unique large pores, these $mSiO_2$ nanospheres acted as effective nanocarriers, exhibiting high protein (bovine β-lactoglobulin)-loading capacity.

Inspired by the previously published work of Zhao and co-workers,[27] herein, we successfully realized a multifunctional nanoplatform based on the deliberately modified large-pore $mSiO_2$ for bimodal imaging, PTT/MHT, and pH/MF/NIR-responsive drug release, as illustrated in Scheme 1. Specifically, Fe_3O_4 NPs of suitable size and PbS/CdS QDs with desired NIR photoluminescence were loaded into the thiol-modified large-pore $mSiO_2$ to form a multifunctional photoluminescent and superparamagnetic nanoplatform ($mSiO_2$@PbS/CdS-Fe_3O_4). Doxorubicin (DOX), a widely used clinical anticancer drug, was used as a model to study their multiresponsive drug-release behavior.[29] The $mSiO_2$@PbS/CdS-Fe_3O_4 as a nanocarrier/host with high loading capacity allows to integrate the unique properties of each component in a single nanoarchitecture. When this nanoplatform was exposed to an acidic tumor microenvironment, pH-responsive drug release was promoted. Under irradiation of NIR light, the PbS/CdS QDs incorporated into the $mSiO_2$@PbS/CdS-Fe_3O_4 not only generated NIR photoluminescence for deep-tissue bioimaging but also converted NIR light to heat for PTT and further triggered or accelerated drug release. Meanwhile, $mSiO_2$@PbS/CdS-Fe_3O_4 consisting of a large number of superparamagnetic Fe_3O_4 NPs were expected to serve as potential MR imaging probes, MHT agents, and effective vehicles for targeted delivery of drugs to cancer sites and to realize promoted MF-responsive drug release.

DOI: 10.1021/acs.chemmater.9b00028
Chem. Mater. 2019, 31, 3201−3210

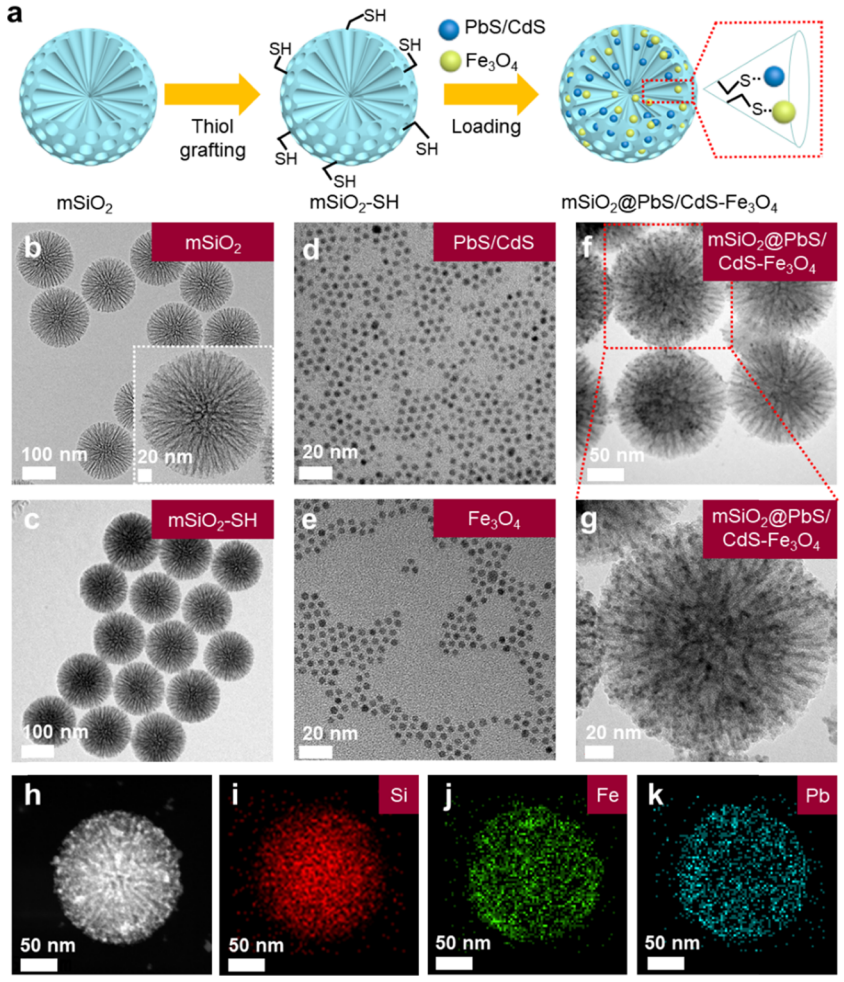

Figure 1. (a) Schematic of the synthetic procedure for $mSiO_2$@PbS/CdS-Fe_3O_4. (b) Transmission electron microscopy (TEM) image of $mSiO_2$. The inset shows the corresponding TEM image of $mSiO_2$ at a higher magnification. (c) TEM images of thiol-modified $mSiO_2$ (denoted as $mSiO_2$-SH herein), (d) PbS/CdS QDs, and (e) Fe_3O_4 NPs. (f, g) TEM images of $mSiO_2$@PbS/CdS-Fe_3O_4 at different magnifications. (h) High-angle annular dark-field scanning transmission electron microscopy (HAADF-STEM) image and (i–k) energy-dispersive X-ray (EDX) elemental mapping images of an individual $mSiO_2$@PbS/CdS-Fe_3O_4.

To the best of our knowledge, this is the first report to simultaneously combine bimodal imaging (NIR deep-tissue photoluminescence and MR imaging), PTT/MHT, and pH/MF/NIR-responsive drug release in one system. This system exhibits three remarkable advantages: (1) multimodal imaging featuring combined preferred NIR deep-tissue photoluminescence and MR imaging; (2) synergistic and highly localized hyperthermia and multiresponsive drug release; and (3) remotely controlled drug release due to the MF/NIR-responsive character. It is expected that such a nanoplatform can be simultaneously used for high efficacy imaging, diagnostics, and therapeutics. The thiol modification, the relatively large pore size, and the rational synthesis of loaded NPs with appropriate sizes are all critical in achieving this complex, highly functional nanostructure.

RESULTS AND DISCUSSION

The synthetic strategy for $mSiO_2$@PbS/CdS-Fe_3O_4 is outlined in Figure 1a, which involves the functionalization of large-pore $mSiO_2$ first with thiol groups using (3-mercaptopropyl)-trimethoxysilane as a coupling agent and subsequent immobilization of Fe_3O_4 NPs and PbS/CdS QDs into thiol-modified nanocarriers ($mSiO_2$). The large-pore $mSiO_2$ was synthesized by a biphase stratification continuous growth approach, i.e., a heterogeneous oil-water biphase stratification reaction system containing tetraethyl orthosilicate in hydrophobic organic solvent of the upper oil phase as well as cationic cetyltrimethylammonium chloride as the template and triethanolamine as the catalyst in the lower aqueous phase.[27] The mesopore size of the nanospheres highly depends on the swelling behavior of the hydrophobic organic solvent in oil-water biphase stratification system. According to the previously published work, $mSiO_2$ with the largest mesopore size of ~13 nm could be obtained when 5% v/v tetraethyl orthosilicate-in-cyclohexane solution was selected as the upper oil phase due to its more effective swelling behavior compared to other organic solvents.[27] Here, since $mSiO_2$ was used as a host for Fe_3O_4 NPs and PbS/CdS QDs, relatively large pore sizes (>10 nm) are in principle preferred for loading more Fe_3O_4 NPs and PbS/CdS QDs. We thus took the same strategy to prepare the $mSiO_2$ with mesopore size >10 nm, as shown in Figure 1b. The resultant large-pore $mSiO_2$ is highly uniform and has a three-dimensional dendritic mesoporous structure with an average size of ca. 170 nm (Figure S1c). Their center-radial mesopore channels can be clearly observed in the inset of Figure 1b. To evaluate the surface area and pore size distribution of $mSiO_2$,

DOI: 10.1021/acs.chemmater.9b00028
Chem. Mater. 2019, 31, 3201–3210

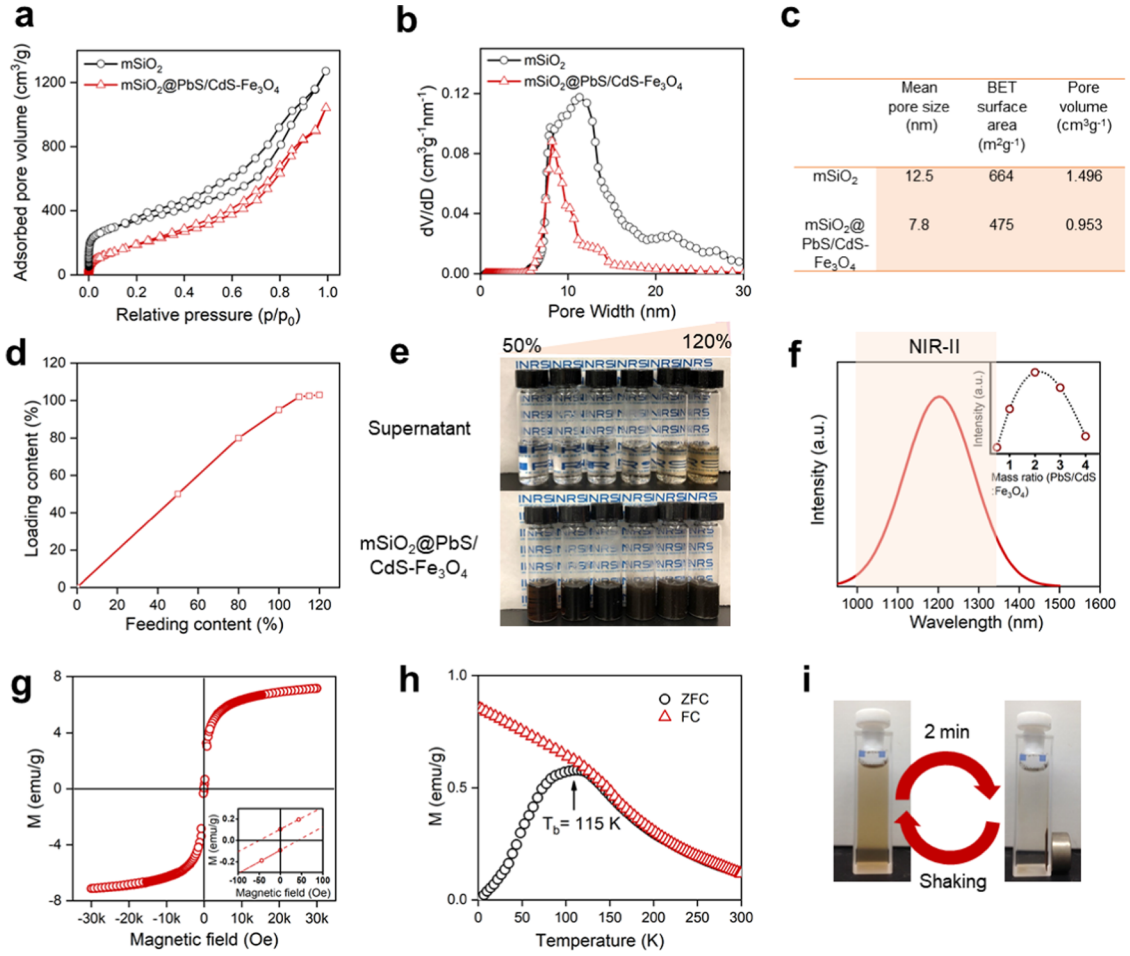

Figure 2. (a) Nitrogen adsorption−desorption isotherms and (b) pore size distribution of $mSiO_2$ and $mSiO_2$@PbS/CdS-Fe_3O_4. (c) Textural properties of $mSiO_2$ and $mSiO_2$@PbS/CdS-Fe_3O_4. (d) Relationship between the measured loading level and feeding content of Fe_3O_4 NPs and PbS/CdS QDs. (e) Photographs of the supernatant (top) and redispersed $mSiO_2$@PbS/CdS-Fe_3O_4 (bottom) after loading Fe_3O_4 NPs and PbS/CdS QDs into thiol-modified $mSiO_2$ with feeding content varied from 50 to 120%. (f) Photoluminescence spectrum of $mSiO_2$@PbS/CdS-Fe_3O_4 in the NIR-II window. The inset shows the corresponding integrated NIR photoluminescence intensity as a function of mass ratio of PbS/CdS QDs to Fe_3O_4 NPs. (g) Field-dependent magnetization of $mSiO_2$@PbS/CdS-Fe_3O_4 at 300 K. The inset shows the enlarged view of field-dependent magnetization curve under low magnetic fields. (h) Temperature-dependent zero-field-cooled (ZFC) and field-cooled (FC) magnetization curves at 100 Oe for $mSiO_2$@PbS/CdS-Fe_3O_4. (i) Photographs of an aqueous dispersion of $mSiO_2$@PbS/CdS-Fe_3O_4 in a cuvette (left) before and (right) after applying a magnet for 2 min. $mSiO_2$@PbS/CdS-Fe_3O_4 can be well redispersed in aqueous solution again after shaking. Logo in (e): used with permission from INRS.

nitrogen adsorption−desorption isotherms (Figure 2a) were acquired by measuring Brunauer−Emmett−Teller (BET) surface adsorption. The isotherms of large-pore $mSiO_2$ can be classified as the type IV isotherm with H4 hysteresis loop, which demonstrates the typical ordered mesoporous structure with a narrow pore size distribution.[30] The BET surface area of $mSiO_2$ was measured to be ∼664 m^2/g and the total pore volume ∼1.496 cm^3/g (Figure 2c). The derived pore size distribution of the $mSiO_2$ is shown in Figure 2b, from which the mean pore size was estimated to be ∼12.5 nm (Figure 2c). It is anticipated that the large pore volume and size of the $mSiO_2$ can provide sufficient space for embedding both Fe_3O_4 NPs and PbS/CdS QDs. The large-pore $mSiO_2$ was subsequently grafted with thiol groups using (3-mercaptopropyl)trimethoxysilane for anchoring Fe_3O_4 NPs and PbS/CdS QDs.[31] The thiol-modified $mSiO_2$ retains the same morphology of $mSiO_2$ (Figure 1c), while the C−H and S−H stretching modes at 2940 and 2560 cm^{-1} in the Fourier transform infrared (FTIR) spectrum (Figure S2) confirm the successful thiol modification of $mSiO_2$.[31]

To easily and efficiently embed Fe_3O_4 NPs and PbS/CdS QDs into the mesoporous channels of the $mSiO_2$, the size of Fe_3O_4 NPs and PbS/CdS QDs should be small enough for loading. Otherwise, these NPs may only be anchored onto the surface of the $mSiO_2$ instead of inside the mesoporous channels and the loading level will be largely restricted. Since PbS/CdS QDs can be synthesized such as to operate in the NIR-II (including both excitation and emission), which is well suited for high-contrast deep-tissue imaging,[32] they have been chosen as the photoluminescent component. Generally, PbS QDs synthesized from the most commonly used sulfur-oleylamine injection method (also used herein) possess sizes in the range of 4.2−6.4 nm.[33−35] After the cation-exchange process, the resultant PbS/CdS QDs maintain a similar size to the initial PbS QDs.[36,37] Their TEM image (Figure 1d) and size distribution histogram (Figure S1a) indicate that the prepared PbS/CdS QDs are 4.3 ± 0.6 nm in diameter and are suitable for loading into the mesopore channels of thiol-modified $mSiO_2$. The emission peak of PbS/CdS QDs is located at 1200 nm in the NIR-II window (Figure S3).

DOI: 10.1021/acs.chemmater.9b00028
Chem. Mater. 2019, 31, 3201−3210

Regarding Fe_3O_4 NPs, high-quality, uniform ones synthesized by the typical thermal decomposition method in 1-octadecene (ODE, boiling point: 320 °C) are usually larger than 10 nm in diameter, which hinders their loading into $mSiO_2$. To circumvent this issue, herein, we have synthesized ultrasmall Fe_3O_4 NPs by a slightly modified thermal decomposition method, in which a mixture of 1-tetradecene/ODE, instead of pure ODE, was employed to lower the boiling point of the solvent (290 °C).[38] The diameter of resulting Fe_3O_4 NPs decreases to ca. 5 nm, which is much smaller than that of Fe_3O_4 NPs synthesized in pure ODE.[38] From their TEM image (Figure 1e) and size distribution histogram (Figure S1b), it can be seen that the ultrasmall Fe_3O_4 NPs have uniform morphology, a narrow size distribution (4.9 ± 0.5 nm), and good dispersity (i.e., no agglomeration), all pertinent for efficient loading inside the thiol-modified $mSiO_2$.

The loading procedure was performed by mixing Fe_3O_4 NPs, PbS/CdS QDs, and the thiol-modified $mSiO_2$ particles in chloroform. The strong coordination between the thiol groups and metal cations resulted in the efficient loading and immobilization of Fe_3O_4 NPs and PbS/CdS QDs inside the mesoporous channels of $mSiO_2$.[31,39] Corresponding TEM images (Figure 1f,g), high-angle annular dark-field scanning transmission electron microscopy (HAADF-STEM) image (Figure 1h), and energy-dispersive X-ray (EDX) elemental mapping images (Figure 1i−k) confirm the loading of Fe_3O_4 NPs and PbS/CdS QDs into thiol-modified $mSiO_2$, and the overall size of $mSiO_2$@PbS/CdS-Fe_3O_4 remains the same as that of the initial $mSiO_2$ (Figure S1d), suggesting that most of the particles are indeed uniformly situated inside the mesoporous channels, instead of residing on the external surface of thiol-modified $mSiO_2$, which is favorable for targeted biomedical applications herein. This conclusion was also supported by BET measurements, to be described in the text later. Meanwhile, the EDX spectra and X-ray diffraction (XRD) patterns (Figure S4a,b) verify that the $mSiO_2$@PbS/CdS-Fe_3O_4 consists of Fe_3O_4 NPs and PbS/CdS QDs. In addition, it should be mentioned that Fe_3O_4 NPs and PbS/CdS QDs cannot be immobilized inside the as-prepared $mSiO_2$ without any surface modification due to the lack of strong interactions between metal cations and SiO_2 (Figure S5). It underlines the critical role of thiol modification, applied herein, in the construction of the multifunctional nanoplatforms of our interest.

We further explored the loading capacity of the mesoporous channels of the $mSiO_2$ matrix. We mixed the Fe_3O_4 NPs and PbS/CdS QDs at a mass ratio of 1:1 and then added them into the thiol-modified $mSiO_2$-in-chloroform dispersion at varying quantities. The loading content (mass ratio of loaded Fe_3O_4 NPs and PbS/CdS QDs to thiol-modified $mSiO_2$ matrix), measured by inductively coupled plasma-optical emission spectrometry, reached 95% (Figure 2d), very close to the nominal feeding content of 100% (mass ratio of added Fe_3O_4 NPs and PbS/CdS QDs to thiol-modified $mSiO_2$). This excellent result was in line with our observation that the supernatant after centrifuging the mixed dispersion was nearly colorless, straightforwardly supporting that not many free, unloaded Fe_3O_4 NPs and PbS/CdS QDs remained in the dispersion (Figure 2e). With a highly porous structure, it is clear that the thiol-modified $mSiO_2$ exhibits a high loading capacity and widely tunable loading levels, which can be adjusted in the range of 0−103% (Figure 2d) by varying the feeding content from 0 to 120%.

It is known that Fe_3O_4 NPs have the photoluminescence quenching effect on QDs, namely, the photoluminescence of QDs decreases in the presence of Fe_3O_4 NPs in a mixed system.[40,41] The details of the photoluminescence quenching mechanism are beyond the scope of the present work. Herein, we fixed the concentration of Fe_3O_4 NPs and then gradually increased the loading concentration of PbS/CdS QDs for the purpose of obtaining the maximum photoluminescence of $mSiO_2$@PbS/CdS-Fe_3O_4 for NIR deep-tissue imaging. It can be observed from TEM images (Figure S6a−c) that significantly more PbS/CdS QDs can be found in the channels of $mSiO_2$@PbS/CdS-Fe_3O_4 with the increased loading of PbS/CdS QDs. The NIR photoluminescence spectrum of $mSiO_2$@PbS/CdS-Fe_3O_4 shows a peak centered at around 1200 nm in the NIR-II window (Figure 2f), which is almost the same as that of the initial PbS/CdS QDs (Figure S3). The NIR photoluminescence intensity of $mSiO_2$@PbS/CdS-Fe_3O_4 first increases with the mass ratio and then decreases mainly due to the self-quenching effect of PbS/CdS QDs at higher concentrations, with the maximum intensity achieved at the mass ratio of 2:1 (Figure 2f). We thus fixed the mass ratio of PbS/CdS QDs to Fe_3O_4 NPs at 2:1 as an optimal value for NIR deep-tissue imaging and used it for the subsequent investigations of this work. After loading with PbS/CdS QDs and Fe_3O_4 NPs, the nitrogen adsorption−desorption isotherms shrink (Figure 2a), which can be easily understood since the mesopores of $mSiO_2$ are now occupied by PbS/CdS QDs and Fe_3O_4 NPs. Similarly, the average pore size becomes smaller and the pore size distribution becomes narrower (Figure 2b), as expected. The average pore size, BET surface area, and pore volume of $mSiO_2$@PbS/CdS-Fe_3O_4 were measured to be ∼7.8 nm, ∼475 m^2/g, and ∼0.953 cm^3/g (Figure 2c), respectively. Although they are all smaller than those of pure $mSiO_2$, as expected, $mSiO_2$@PbS/CdS-Fe_3O_4 still has sufficient space for loading drug molecules because of their unique three-dimensional dendritic mesoporous structure.

Since the ultrasmall Fe_3O_4 NPs are embedded into the mesopores of $mSiO_2$, the $mSiO_2$@PbS/CdS-Fe_3O_4 possesses interesting superparamagnetic properties. The magnetic characterization was performed using a vibrating sample magnetometer. The field-dependent magnetization plot with negligible remanence and coercivity shown in Figure 2g illustrates that $mSiO_2$@PbS/CdS-Fe_3O_4 is superparamagnetic with a saturation magnetization (M_s) of ∼7.1 emu/g at 300 K. This value is lower than those reported for plain Fe_3O_4 NPs in the literature because the presence of nonmagnetic components of thiol-modified $mSiO_2$ and PbS/CdS QDs inside $mSiO_2$@PbS/CdS-Fe_3O_4 reduces the "magnetically effective" weight, and thus decreases the value of Ms per gram of $mSiO_2$@PbS/CdS-Fe_3O_4. The temperature-dependent zero-field-cooled (ZFC) and field-cooled (FC) magnetization curves of $mSiO_2$@PbS/CdS-Fe_3O_4 (Figure 2h) were measured under a magnetic field of 100 Oe between 5 and 300 K. The ZFC and FC curves coincide at high temperatures but diverge at low temperatures due to progressive blocking of particles as the temperature decreases, which is consistent with the characteristic superparamagnetic behavior.[42,43] The blocking temperature (T_b) was estimated to be ∼115 K, lower than room temperature, suggesting the superparamagnetic behavior of $mSiO_2$@PbS/CdS-Fe_3O_4 at room temperature and further ensuring its easy manipulation by an external MF at room temperature. As a consequence, the complex $mSiO_2$@PbS/CdS-Fe_3O_4 particles well dispersed in an aqueous solution

DOI: 10.1021/acs.chemmater.9b00028
Chem. Mater. 2019, 31, 3201−3210

(Figure 2i, left) can be rapidly confined toward a magnet in 2 min after it is applied (Figure 2i, right). Slight shaking of the cuvette will redisperse the $mSiO_2$@PbS/CdS-Fe_3O_4 back into the original solution after removing the magnet. The easy confinement and redispersion of the $mSiO_2$@PbS/CdS-Fe_3O_4 is reversible and can be repeated many times. Unlike classic ferromagnetic NPs that will form nonseparable agglomerates after initial magnetic confinement, the superparamagnetic, redispersible behavior of these $mSiO_2$@PbS/CdS-Fe_3O_4 particles is undoubtedly very important for magnetically driven biomedical applications, such as bioseparation and site-specific targeting.[44]

As mentioned above, $mSiO_2$@PbS/CdS-Fe_3O_4 exhibits strong photoluminescence in the NIR-II window, which is a merit for deep-tissue bioimaging. To demonstrate the use of $mSiO_2$@PbS/CdS-Fe_3O_4 particles as a bioprobe for deep-tissue imaging, we designed an ex vivo setup to examine their NIR photoluminescence penetration capability (Figure 3a).

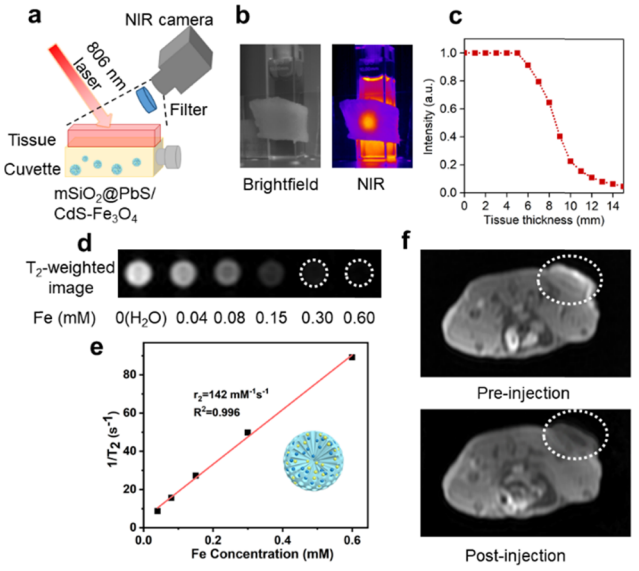

Figure 3. (a) Scheme of the experimental setup for the deep-tissue NIR photoluminescence imaging of $mSiO_2$@PbS/CdS-Fe_3O_4. (b) The corresponding bright-field and NIR photoluminescence images of $mSiO_2$@PbS/CdS-Fe_3O_4 in the cuvette covered with tissue. The bright-field image was acquired under indoor light without any filters in the optical path. The NIR photoluminescence image was recorded upon excitation with an 806 nm laser, along with an 830 nm long-pass filter. (c) Normalized photoluminescence intensity of the $mSiO_2$@PbS/CdS-Fe_3O_4 measured from the NIR images as a function of tissue thickness. (d) T_2-weighted MR images of $mSiO_2$@PbS/CdS-Fe_3O_4 with various Fe concentrations. (e) Relaxation rate r_2 ($1/T_2$) vs different molar Fe concentrations of $mSiO_2$@PbS/CdS-Fe_3O_4. (f) In vivo T_2-weighted transversal cross-sectional MR imaging of nude mouse bearing a tumor acquired at pre-injection and 30 min intratumoral post-injection of $mSiO_2$@PbS/CdS-Fe_3O_4 at 1.5 mg/kg. The position of the tumor was marked by white dashed circles.

Briefly, an 806 nm laser with power density of 10 W/cm^2 was used to excite the $mSiO_2$@PbS/CdS-Fe_3O_4 aqueous dispersion in a cuvette through a piece of pork tissue, while the NIR camera equipped with an 830 nm optical long-pass filter was fixed above the tissue to collect the emitted NIR signal. The use of the 806 nm laser as an excitation source not only provides enhanced penetration depth, compared to excitation wavelengths around 1000 nm, but also reduces the thermal load in the area of interest and thus minimizes potential damage to healthy biological tissues.[13,45] Figure 3b shows the bright-field and NIR photoluminescence images of $mSiO_2$@PbS/CdS-Fe_3O_4 in the cuvette covered with the pork tissue. Intense NIR photoluminescence can be seen in the center of pork tissue, which is larger than the size of the excitation beam due to the scattering of both the excitation and emitted lights as they pass through the tissue. By changing the thickness of the pork tissue, we can evaluate the NIR photoluminescence penetration depth from the normalized photoluminescence intensity of the $mSiO_2$@PbS/CdS-Fe_3O_4 in the aqueous solution, as illustrated in Figure 3c. The intensity of the photoluminescence signal saturates the detector of the NIR camera when the thickness of the pork tissue is ≤5 mm. After that, with increasing thickness of the pork tissue (>5 mm), the signal gradually diminishes. With this setup, a maximum penetration depth of approximately 14 mm was obtained using $mSiO_2$@PbS/CdS-Fe_3O_4.

Prior to performing in vivo MR imaging studies, we assessed the biocompatibility of $mSiO_2$@PbS/CdS-Fe_3O_4 in vitro using HeLa cancer cells and human embryonic kidney (HEK 293T) cells. As shown in Figure S7, after being incubated with $mSiO_2$@PbS/CdS-Fe_3O_4 for 24 h, both HeLa and HEK 293T cells retained more than 70% viability even at the high particle concentration up to 250 μg/mL. Inspired by their excellent superparamagnetic properties, we next examined their use as T_2 contrast agents for MR imaging. The in vitro T_2-weighted MR images of $mSiO_2$@PbS/CdS-Fe_3O_4 with various Fe concentrations are shown in Figure 3d, which clearly demonstrates the characteristic concentration-dependent negative enhancement effect on T_2 MR imaging. That is, the images of $mSiO_2$@PbS/CdS-Fe_3O_4 dispersions are gradually getting darker with increasing Fe concentration in dispersions, whereas the particle-free sample remains bright. The T_2 relaxivity coefficient (r_2) of $mSiO_2$@PbS/CdS-Fe_3O_4 could be calculated from the fitting curve of T_2 versus Fe concentration (Figure 3e), and was determined to be approximately 142 mM^{-1} s^{-1}, which is almost twice that of Ferumoxsil (r_2 = 72 mM^{-1} s^{-1}, one of the clinically approved Fe-based MR imaging contrast agents).[46] The short distance between Fe_3O_4 NPs located in the mesoporous channel of the $mSiO_2$ might permit magnetic coupling between the magnetic NPs, resulting in a synergistic increase in r_2.[47] This value is not only higher than that (61 mM^{-1} s^{-1}) of our previously reported single-core Fe_3O_4@SiO_2@$NaYF_4$:Nd^{3+} nanoplatform, but also comparable to those of multi-magnetic-core NPs for MR imaging reported in the literature.[7,48−50] Considering the excellent in vitro MR imaging capability of $mSiO_2$@PbS/CdS-Fe_3O_4 particles, we further explored their potential as a negative contrast agent for in vivo MR imaging. A mouse bearing a tumor was imaged by a 3.0 T clinical MR scanner at pre-injection and 30 min after intratumoral injection of $mSiO_2$@PbS/CdS-Fe_3O_4 (200 μL, 2 mg/mL, dose = 1.5 mg/kg), as shown in Figure 3f. The tumor area of the mouse appears bright before the injection of $mSiO_2$@PbS/CdS-Fe_3O_4, while a remarkable darkening effect in the tumor site can be observed at 30 min post-injection (white dashed circles in Figure 3f). This significant T_2 negative effect makes $mSiO_2$@PbS/CdS-Fe_3O_4 ideal as a highly efficient T_2 contrast agent for MR imaging. Combined with excellent deep-tissue NIR photoluminescence penetration capacity, these experimental results reveal that $mSiO_2$@PbS/CdS-Fe_3O_4 can serve

DOI: 10.1021/acs.chemmater.9b00028
Chem. Mater. 2019, 31, 3201−3210

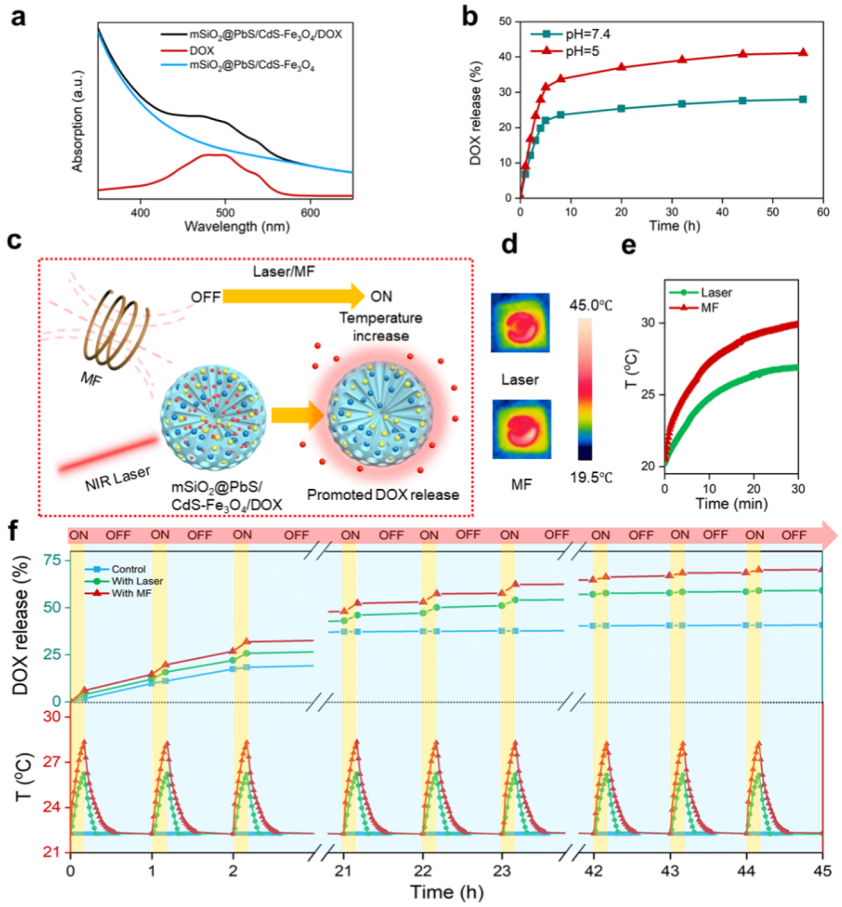

Figure 4. (a) Absorption spectra of free DOX, $mSiO_2$@PbS/CdS-Fe_3O_4, and DOX-loaded $mSiO_2$@PbS/CdS-Fe_3O_4 ($mSiO_2$@PbS/CdS-Fe_3O_4/DOX). (b) DOX release profile of $mSiO_2$@PbS/CdS-Fe_3O_4/DOX at pH = 7.4 and 5. (c) Schematic illustration of PTT/MHT and heat-induced DOX release in response to the external laser and MF. (d) Thermal images of $mSiO_2$@PbS/CdS-Fe_3O_4 solution after 30 min of two types of modulation (laser at 1.3 W/cm^2, MF at 5 kA/m). (e) Corresponding time-dependent temperature curves of $mSiO_2$@PbS/CdS-Fe_3O_4 (0.4 mg in a total volume of 2 mL) solution. (f) DOX release profiles of $mSiO_2$@PbS/CdS-Fe_3O_4/DOX dispersion (0.2 mg/mL, 2 mL) stimulated by laser/MF (top) and the time evolution of the corresponding temperature of the solution (bottom); the $mSiO_2$@PbS/CdS-Fe_3O_4/DOX dispersion under no stimulation, i.e., without the use of the laser or MF, is shown as a control. The laser and MF were switched between "ON" and "OFF" modes.

as a promising and powerful bimodal (photoluminescence and MR) imaging probe in vivo.

To investigate their potential as drug-delivery carriers, DOX was selected as a model drug to load into $mSiO_2$@PbS/CdS-Fe_3O_4. There are not any obvious peaks in the absorption spectrum of $mSiO_2$@PbS/CdS-Fe_3O_4 before drug loading, while an absorption peak located at ~480 nm can be clearly found after DOX loading, which is the characteristic absorption peak of DOX (Figure 4a). Hence, the loading efficiency of DOX can be calculated by monitoring the absorption intensity at 480 nm (the details of calibration of DOX loading are shown in Figure S8). In our case, the loading efficiency of DOX for $mSiO_2$@PbS/CdS-Fe_3O_4 was calculated to be about 36.4%, lower than that (71%) of plain $mSiO_2$, which is due to the fact that the integrated Fe_3O_4 NPs and PbS/CdS QDs occupy considerable space in the mesoporous channels of the $mSiO_2$ (as supported by BET measurements) and block the DOX molecules from easily accessing the mesopores. It has been known that the extracellular pH value of normal cells is close to neutral, but the presence of cancer cells increases the acidity of their microenvironments due to the excess metabolic products in the rapid proliferation of cancer cells.[51,52] The different pH values between normal tissues and cancer cellular environment may provide an additional safe and efficient physiological stimulus for pH-responsive and target-specific drug delivery. In this way, the drug release can be inhibited during systemic circulation of drug carriers at a physiological pH value of 7.4, while it is enhanced in the acidic environment at tumor sites. Thus, pH-sensitive nanoplatform, like $mSiO_2$@PbS/CdS-Fe_3O_4/DOX, is appealing and highly desirable to reduce overdose-induced side effects of traditional nonspecific chemotherapy. Considering this factor, we studied the DOX release behavior from $mSiO_2$@PbS/CdS-Fe_3O_4/DOX in phosphate-buffered saline (PBS) at two different pH values (pH = 7.4 and 5), as illustrated in Figure 4b. Both profiles show fast release of DOX in the first 4 h, followed by a slow release over 8 h. These different release rates can be reasonably explained by the different loading locations of DOX inside $mSiO_2$@PbS/CdS-Fe_3O_4. To be more specific, the DOX molecules situated in the outer mesoporous channels or on the external silica surface are easily released at the beginning, while the DOX molecules loaded into the inner channels require longer time to diffuse from inside to outside. This behavior is beneficial for targeted drug release since the initially fast release can efficiently inhibit the growth of cancer cells and then the slow release of the rest of drugs can further curb the surviving cancer cells.[53] In addition, the DOX release profile of $mSiO_2$@PbS/CdS-Fe_3O_4/

DOI: 10.1021/acs.chemmater.9b00028
Chem. Mater. 2019, 31, 3201−3210

DOX shows pH-dependent behavior: the DOX release reaches 41% after 56 h at pH = 5, while it only increases to 28% at pH = 7.4. The higher drug release can be ascribed to the enhanced hydrophilicity and higher solubility of DOX by increased protonation of NH_2 groups of DOX at lower pH values. This clear pH-sensitive drug release behavior is advantageous for localized cancer chemotherapy.

We then further studied the PTT and MHT of $mSiO_2$@PbS/CdS-Fe_3O_4 under external stimuli of the NIR laser and MF, respectively, and their effect on the DOX release behavior (Figure 4c). The thermal images of $mSiO_2$@PbS/CdS-Fe_3O_4 dispersion (0.2 mg/mL) after 30 min of two types of modulation (laser at 1.3 W/cm^2, MF at 5 kA/m) and time-dependent temperature curves of $mSiO_2$@PbS/CdS-Fe_3O_4 solution are shown in Figure 4d,e, respectively. The temperature of $mSiO_2$@PbS/CdS-Fe_3O_4 dispersion after 30 min heating by the NIR laser and MF increases by 6.7 and 9.5 °C, respectively, while the PBS solution alone shows negligible temperature increase under the same modulation (Figure S9). This result clearly confirms that the temperature increase is attributed to the response of $mSiO_2$@PbS/CdS-Fe_3O_4 to the external laser/MF and suggests their high potential as PTT/MHT agents. Subsequently, the MF/NIR-responsive drug release of DOX from the $mSiO_2$@PbS/CdS-Fe_3O_4/DOX particles was examined (Figure 4f). The dispersion was stimulated with the MF or NIR laser (ON) for 10 min, followed by a 50 min interval with MF/NIR being switched OFF. The "ON/OFF" cycles were performed in a 45 h period, and the time evolution of the temperature of the dispersion was recorded at the same time. Meanwhile, an $mSiO_2$@PbS/CdS-Fe_3O_4/DOX dispersion without being stimulated by the laser/MF was shown as a control. The release of DOX is increased when the NIR/MF is ON. When the NIR/MF is switched OFF, the drug-release rate returns back to the regular value, similar to that of the control. The temperature curves under the ON/OFF mode show the similar trend to the drug-release profile, which means that the surge of DOX release is ascribed to the local heating effect produced by the external stimuli of NIR/MF (Figure 4c). The total release amount of DOX reached 59 and 70% after 45 h under NIR/MF, respectively, compared to 40% in the control experiment. Given their excellent magnetothermal and photothermal conversion effect of $mSiO_2$@PbS/CdS-Fe_3O_4, this nanoplatform should be an ideal candidate for PTT/MHT and a new efficient drug carrier for MF/NIR-responsive drug release.

CONCLUSIONS

In summary, we have successfully prepared a multifunctional nanoplatform ($mSiO_2$@PbS/CdS-Fe_3O_4), which integrated NIR photoluminescent PbS/CdS QDs and superparamagnetic Fe_3O_4 NPs into a large-pore silica matrix enabled by simple thiol modification. The $mSiO_2$@PbS/CdS-Fe_3O_4 exhibited excellent photoluminescence in the NIR-II window, enabling its use for deep-tissue imaging, as well as excellent superparamagnetic properties that make it easily confined by an external MF and ideal as a highly efficient T_2 contrast agent for MR imaging in vivo. In particular, it showed an extremely high r_2 value due to the synergistic magnetic coupling effect induced by close distance of Fe_3O_4 NPs embedded in the mesoporous channel. This nanoplatform also demonstrated a great potential as a drug-delivery carrier for cancer therapy. After being loaded with DOX, in addition to showing pH-responsive drug-release behavior, $mSiO_2$@PbS/CdS-Fe_3O_4 can produce local heat via the magnetothermal effect, thanks to the presence of superparamagnetic NPs, and accelerate the drug release. Furthermore, benefitting from the presence of the NIR-absorbing QDs, $mSiO_2$@PbS/CdS-Fe_3O_4 can not only serve as a highly efficient PTT agent but also increase the drug-release rate under NIR irradiation. This nanoplatform thus yields a synergistic effect from the integrated heating mode and multiresponsive drug release to achieve a high therapeutic efficacy. Such specifically designed multifunctional nanoplatform combining bimodal imaging (NIR deep-tissue photoluminescence and MR imaging), PTT/MHT, and pH/MF/NIR-responsive drug release has a great potential for cancer imaging diagnostics and therapeutics.

ASSOCIATED CONTENT

Supporting Information

The Supporting Information is available free of charge on the ACS Publications website at DOI: 10.1021/acs.chemmater.9b00028.

Experimental section; size distribution of PbS/CdS QDs, Fe_3O_4 NPs, $mSiO_2$, and $mSiO_2$@PbS/CdS-Fe_3O_4; FTIR spectra of $mSiO_2$ and $mSiO_2$-SH; photoluminescence spectrum of PbS/CdS QDs; EDX spectra and XRD patterns of $mSiO_2$ and $mSiO_2$@PbS/CdS-Fe_3O_4; TEM images of pure $mSiO_2$ loaded with Fe_3O_4 NPs and PbS/CdS QDs; TEM images of $mSiO_2$@PbS/CdS-Fe_3O_4 with various loading ratios of PbS/CdS QDs and Fe_3O_4 NPs; cytotoxicity study of $mSiO_2$@PbS/CdS-Fe_3O_4; DOX calibration; and temperature curves of PBS solution under laser/MF (PDF)

AUTHOR INFORMATION

Corresponding Authors

*E-mail: vetrone@emt.inrs.ca (F.V.).
*E-mail: ma@emt.inrs.ca (D.M.).

ORCID

Fan Yang: 0000-0001-6306-4501
Artiom Skripka: 0000-0003-4060-4290
Jung Kwon Oh: 0000-0002-4220-308X
Xinyu Liu: 0000-0001-5705-9765
Fiorenzo Vetrone: 0000-0002-3222-3052
Dongling Ma: 0000-0001-8558-3150

Notes

The authors declare no competing financial interest.

ACKNOWLEDGMENTS

D.M. and F.V. are grateful to the Natural Sciences and Engineering Research Council of Canada (NSERC: RGPIN-2015-06756) and the Fonds de Recherche du Québec—Nature et technologies (FRQNT: 2014-PR-174462) for funding. F.Y., F.R., and A.S. greatly appreciate the financial support from the Merit Scholarship Program for Foreign Students from the Ministère de l'Éducation, du Loisir et du Sport du Québec (Nos. 193353, 255072, and 257149).

REFERENCES

(1) Liu, C.; Gao, Z.; Zeng, J.; Hou, Y.; Fang, F.; Li, Y.; Qiao, R.; Shen, L.; Lei, H.; Yang, W.; Gao, M. Magnetic/Upconversion Fluorescent $NaGdF_4$:Yb,Er Nanoparticle-Based Dual-Modal Molecular Probes for Imaging Tiny Tumors *In Vivo*. *ACS Nano* **2013**, *7*, 7227−7240.

DOI: 10.1021/acs.chemmater.9b00028
Chem. Mater. 2019, 31, 3201−3210

(2) Lee, J.; Jun, Y.; Yeon, S.; Shin, J.; Cheon, J. Dual-Mode Nanoparticle Probes for High-Performance Magnetic Resonance and Fluorescence Imaging of Neuroblastoma. *Angew. Chem., Int. Ed.* **2006**, *45*, 8160−8162.
(3) Chen, O.; Riedemann, L.; Etoc, F.; Herrmann, H.; Coppey, M.; Barch, M.; Farrar, C. T.; Zhao, J.; Bruns, O. T.; Wei, H.; Guo, P.; Cui, J.; Jensen, R.; Chen, Y.; Harris, D. K.; Cordero, J. M.; Wang, Z.; Jasanoff, A.; Fukumura, D.; Reimer, R.; Dahan, M.; Jain, R. K.; Bawendi, M. G. Magneto-Fluorescent Core-Shell Supernanoparticles. *Nat. Commun.* **2014**, *5*, No. 5093.
(4) Cheng, L.; Wang, C.; Ma, X.; Wang, Q.; Cheng, Y.; Wang, H.; Li, Y.; Liu, Z. Multifunctional Upconversion Nanoparticles for Dual-Modal Imaging-Guided Stem Cell Therapy under Remote Magnetic Control. *Adv. Funct. Mater.* **2013**, *23*, 272−280.
(5) Zhang, L.; Wang, Y.; Yang, Y.; Zhang, F.; Dong, W.; Zhou, S.; Pei, W.; Chen, H.; Sun, H. Magnetic/Upconversion Luminescent Mesoparticles of Fe_3O_4@LaF_3:Yb^{3+}, Er^{3+} for Dual-Modal Bioimaging. *Chem. Commun.* **2012**, *48*, 11238−11240.
(6) Zhu, X.; Zhou, J.; Chen, M.; Shi, M.; Feng, W.; Li, F. Core-Shell Fe_3O_4@$NaLuF_4$:Yb,Er/Tm Nanostructure for MRI, CT and Upconversion Luminescence Tri-Modality Imaging. *Biomaterials* **2012**, *33*, 4618−4627.
(7) Yang, F.; Skripka, A.; Benayas, A.; Dong, X.; Hong, S. H.; Ren, F.; Oh, J. K.; Liu, X.; Vetrone, F.; Ma, D. An Integrated Multifunctional Nanoplatform for Deep-Tissue Dual-Mode Imaging. *Adv. Funct. Mater.* **2018**, *28*, No. 1706235.
(8) Part, F.; Zaba, C.; Bixner, O.; Grünewald, T. A.; Michor, H.; Küpcü, S.; Debreczeny, M.; De Vito Francesco, E.; Lassenberger, A.; Schrittwieser, S.; et al. The Doping Method Determines Para-or Superparamagnetic Properties of Photostable and Surface Modifiable Quantum Dots for Multimodal Bioimaging. *Chem. Mater.* **2018**, *30*, 4233−4241.
(9) Pahari, S. K.; Olszakier, S.; Kahn, I.; Amirav, L. Magneto-Fluorescent Yolk-Shell Nanoparticles. *Chem. Mater.* **2018**, *30*, 775−780.
(10) Ma, D.; Guan, J.; Dénommée, S.; Enright, G.; Veres, T.; Simard, B. Multifunctional Nano-Architecture for Biomedical Applications. *Chem. Mater.* **2006**, *18*, 1920−1927.
(11) Zhang, F.; Braun, G. B.; Pallaoro, A.; Zhang, Y.; Shi, Y.; Cui, D.; Moskovits, M.; Zhao, D.; Stucky, G. D. Mesoporous Multifunctional Upconversion Luminescent and Magnetic "Nanorattle" Materials for Targeted Chemotherapy. *Nano Lett.* **2012**, *12*, 61−67.
(12) Shi, D.; Cho, H. S.; Chen, Y.; Xu, H.; Gu, H.; Lian, J.; Wang, W.; Liu, G.; Huth, C.; Wang, L.; Ewing, R. C.; Budko, S.; Pauletti, G. M.; Dong, Z. Fluorescent Polystyrene-Fe_3O_4 Composite Nanospheres for *In Vivo* Imaging and Hyperthermia. *Adv. Mater.* **2009**, *21*, 2170−2173.
(13) Hemmer, E.; Benayas, A.; Legare, F.; Vetrone, F. Exploiting the Biological Windows: Current Perspectives on Fluorescent Bioprobes Emitting above 1000 nm. *Nanoscale Horiz.* **2016**, *1*, 168−184.
(14) Skripka, A.; Karabanovas, V.; Jarockyte, G.; Marin, R.; Tam, V.; Cerruti, M.; Rotomskis, R.; Vetrone, F. Decoupling Theranostics with Rare Earth Doped Nanoparticles. *Adv. Funct. Mater.* **2019**, *29*, No. 1807105.
(15) Chinen, A. B.; Guan, C. M.; Ferrer, J. R.; Barnaby, S. N.; Merkel, T. J.; Mirkin, C. A. Nanoparticle Probes for the Detection of Cancer Biomarkers, Cells, and Tissues by Fluorescence. *Chem. Rev.* **2015**, *115*, 10530−10574.
(16) Liu, B.; Li, C.; Ma, P.; Chen, Y.; Zhang, Y.; Hou, Z.; Huang, S.; Lin, J. Multifunctional $NaYF_4$:Yb,Er@$mSiO_2$@Fe_3O_4-PEG nanoparticles for UCL/MR bioimaging and magnetically targeted drug delivery. *Nanoscale* **2015**, *7*, 1839−1848.
(17) Cheng, R.; Meng, F.; Deng, C.; Klok, H.; Zhong, Z. Dual and Multi-Stimuli Responsive Polymeric Nanoparticles for Programmed Site-Specific Drug Delivery. *Biomaterials* **2013**, *34*, 3647−3657.
(18) Wang, C.; Xu, H.; Liang, C.; Liu, Y.; Li, Z.; Yang, G.; Cheng, L.; Li, Y.; Liu, Z. Iron Oxide@Polypyrrole Nanoparticles as a Multifunctional Drug Carrier for Remotely Controlled Cancer Therapy with Synergistic Antitumor Effect. *ACS Nano* **2013**, *7*, 6782−6795.
(19) Jing, L.; Liang, X.; Li, X.; Lin, L.; Yang, Y.; Yue, X.; Dai, Z. Mn-Porphyrin Conjugated Au Nanoshells Encapsulating Doxorubicin for Potential Magnetic Resonance Imaging and Light Triggered Synergistic Therapy of Cancer. *Theranostics* **2014**, *4*, 858.
(20) Kang, X.; Cheng, Z.; Yang, D.; Ma, P.; Shang, M.; Peng, C.; Dai, Y.; Lin, J. Design and Synthesis of Multifunctional Drug Carriers Based on Luminescent Rattle-Type Mesoporous Silica Microspheres with a Thermosensitive Hydrogel as a Controlled Switch. *Adv. Funct. Mater.* **2012**, *22*, 1470−1481.
(21) Chiang, W. L.; Ke, C. J.; Liao, Z. X.; Chen, S. Y.; Chen, F. R.; Tsai, C. Y.; Xia, Y.; Sung, H. W. Pulsatile Drug Release from PLGA Hollow Microspheres by Controlling the Permeability of Their Walls with a Magnetic Field. *Small* **2012**, *8*, 3584−3588.
(22) Liu, J.; Wang, C.; Wang, X.; Wang, X.; Cheng, L.; Li, Y.; Liu, Z. Mesoporous Silica Coated Single-Walled Carbon Nanotubes as a Multifunctional Light-Responsive Platform for Cancer Combination Therapy. *Adv. Funct. Mater.* **2015**, *25*, 384−392.
(23) Wang, H.; Cao, G.; Gai, Z.; Hong, K.; Banerjee, P.; Zhou, S. Magnetic/NIR-Responsive Drug Carrier, Multicolor Cell Imaging, and Enhanced Photothermal Therapy of Gold Capped Magnetite-Fluorescent Carbon Hybrid Nanoparticles. *Nanoscale* **2015**, *7*, 7885−7895.
(24) Kurapati, R.; Raichur, A. M. Near-Infrared Light-Responsive Graphene Oxide Composite Multilayer Capsules: A Novel Route for Remote Controlled Drug Delivery. *Chem. Commun.* **2013**, *49*, 734−736.
(25) Sumer, B.; Gao, J. Theranostic Nanomedicine for Cancer. *Nanomedicine* **2008**, *3*, 137−140.
(26) Chen, Y.; Gao, Y.; Chen, H.; Zeng, D.; Li, Y.; Zheng, Y.; Li, F.; Ji, X.; Wang, X.; Chen, F.; et al. Engineering Inorganic Nanoemulsions/Nanoliposomes by Fluoride-Silica Chemistry for Efficient Delivery/Co-Delivery of Hydrophobic Agents. *Adv. Funct. Mater.* **2012**, *22*, 1586−1597.
(27) Shen, D.; Yang, J.; Li, X.; Zhou, L.; Zhang, R.; Li, W.; Chen, L.; Wang, R.; Zhang, F.; Zhao, D. Biphase Stratification Approach to Three-Dimensional Dendritic Biodegradable Mesoporous Silica Nanospheres. *Nano Lett.* **2014**, *14*, 923−932.
(28) Niu, D.; Liu, Z.; Li, Y.; Luo, X.; Zhang, J.; Gong, J.; Shi, J. Monodispersed and Ordered Large-Pore Mesoporous Silica Nanospheres with Tunable Pore Structure for Magnetic Functionalization and Gene Delivery. *Adv. Mater.* **2014**, *26*, 4947−4953.
(29) Cheng, Z.; Ma, P.; Hou, Z.; Wang, W.; Dai, Y.; Zhai, X.; Lin, J. YVO_4:Eu^{3+} Functionalized Porous Silica Submicrospheres as Delivery Carriers of Doxorubicin. *Dalton Trans.* **2012**, *41*, 1481−1489.
(30) Sangwichien, C.; Aranovich, G.; Donohue, M. Density Functional Theory Predictions of Adsorption Isotherms with Hysteresis Loops. *Colloids Surf., A* **2002**, *206*, 313−320.
(31) Lu, Z.; Gao, C.; Zhang, Q.; Chi, M.; Howe, J. Y.; Yin, Y. Direct Assembly of Hydrophobic Nanoparticles to Multifunctional Structures. *Nano Lett.* **2011**, *11*, 3404−3412.
(32) Benayas, A.; Ren, F.; Carrasco, E.; Marzal, V.; del Rosal, B.; Gonfa, B. A.; Juarranz, Á.; Sanz-Rodríguez, F.; Jaque, D.; García-Solé, J.; Ma, D.; Vetrone, F. PbS/CdS/ZnS Quantum Dots: A Multifunctional Platform for *In Vivo* Near-Infrared Low-Dose Fluorescence Imaging. *Adv. Funct. Mater.* **2015**, *25*, 6650−6659.
(33) Tan, L.; Zhou, Y.; Ren, F.; Benetti, D.; Yang, F.; Zhao, H.; Rosei, F.; Chaker, M.; Ma, D. Ultrasmall PbS Quantum Dots: a Facile and Greener Synthetic Route and Their High Performance in Luminescent Solar Concentrators. *J. Mater. Chem. A* **2017**, *5*, 10250−10260.
(34) Ren, F.; del Rosal, B.; An, S. Y.; Yang, F.; Carrasco, E.; Benayas, A.; Oh, J. K.; Jaque, D.; de la Fuente, ÁJ.; Vetrone, F.; Ma, D. Development and Investigation of Ultrastable PbS/CdS/ZnS Quantum Dots for Near-Infrared Tumor Imaging. *Part. Part. Syst. Charact.* **2017**, *34*, No. 1600242.

DOI: 10.1021/acs.chemmater.9b00028
Chem. Mater. 2019, 31, 3201−3210

(35) Xu, Z.; Liu, Y.; Ren, F.; Yang, F.; Ma, D. Development of Functional Nanostructures and Their Applications in Catalysis and Solar Cells. *Coord. Chem. Rev.* **2016**, *320*−*321*, 153−180.
(36) Ren, F.; Lindley, S. A.; Zhao, H.; Tan, L.; Gonfa, B.; Pu, Y.; Yang, F.; Liu, X.; Vidal, F.; Zhang, J.; Vetrone, F.; Ma, D. Towards Understanding the Unusual Photoluminescence Intensity Variation of Ultrasmall Colloidal PbS Quantum Dots with the Formation of a Thin CdS Shell. *Phys. Chem. Chem. Phys.* **2016**, *18*, 31828−31835.
(37) Tan, L.; Yang, F.; Kim, M. R.; Li, P.; Gangadharan, D. T.; Margot, J.; Izquierdo, R.; Chaker, M.; Ma, D. Enhanced Long-term and Thermal Stability of Polymer Solar Cells in Air at High Humidity with the Formation of Unusual Quantum Dot Networks. *ACS Appl. Mater. Interfaces* **2017**, *9*, 26257−26267.
(38) Lynch, J.; Zhuang, J.; Wang, T.; LaMontagne, D.; Wu, H.; Cao, Y. C. Gas-Bubble Effects on the Formation of Colloidal Iron Oxide Nanocrystals. *J. Am. Chem. Soc.* **2011**, *133*, 12664−12674.
(39) Huang, L.; Liao, T.; Wang, J.; Ao, L.; Su, W.; Hu, J. Brilliant Pitaya-Type Silica Colloids with Central-Radial and High-Density Quantum Dots Incorporation for Ultrasensitive Fluorescence Immunoassays. *Adv. Funct. Mater.* **2018**, *28*, No. 1705380.
(40) Erogbogbo, F.; Yong, K.; Hu, R.; Law, W.; Ding, H.; Chang, C.; Prasad, P. N.; Swihart, M. T. Biocompatible Magnetofluorescent Probes: Luminescent Silicon Quantum Dots Coupled with Superparamagnetic Iron (III) Oxide. *ACS Nano* **2010**, *4*, 5131−5138.
(41) Sathe, T. R.; Agrawal, A.; Nie, S. Mesoporous Silica Beads Embedded with Semiconductor Quantum Dots and Iron Oxide Nanocrystals: Dual-Function Microcarriers for Optical Encoding and Magnetic Separation. *Anal. Chem.* **2006**, *78*, 5627−5632.
(42) Hansen, M. F.; Mørup, S. Estimation of Blocking Temperatures from ZFC/FC Curves. *J. Magn. Magn. Mater.* **1999**, *203*, 214−216.
(43) Cannas, C.; Casula, M. F.; Concas, G.; Corrias, A.; Gatteschi, D.; Falqui, A.; Musinu, A.; Sangregorio, C.; Spano, G. Magnetic Properties of γ-Fe_2O_3-SiO_2 Aerogel and Xerogel Nanocomposite Materials. *J. Mater. Chem.* **2001**, *11*, 3180−3187.
(44) Sung Lee, J.; Myung Cha, J.; Young Yoon, H.; Lee, J.; Keun Kim, Y. Magnetic Multi-Granule Nanoclusters: A Model System That Exhibits Universal Size Effect of Magnetic Coercivity. *Sci. Rep.* **2015**, *5*, No. 12135.
(45) Yang, F.; Skripka, A.; Tabatabaei, M. S.; Hong, S. H.; Ren, F.; Benayas, A.; Oh, J. K.; Martel, S.; Liu, X.; Vetrone, F.; Ma, D. Multifunctional Self-Assembled Supernanoparticles for Deep-Tissue Bimodal Imaging and Amplified Dual-Mode Heating Treatment. *ACS Nano* **2019**, *13*, 408−420.
(46) Zhao, H.; Zou, Q.; Sun, S.; Yu, C.; Zhang, X.; Li, R.; Fu, Y. Theranostic Metal-Organic Framework Core-Shell Composites for Magnetic Resonance Imaging and Drug Delivery. *Chem. Sci.* **2016**, *7*, 5294−5301.
(47) Yang, X.; Grailer, J. J.; Rowland, I. J.; Javadi, A.; Hurley, S. A.; Matson, V. Z.; Steeber, D. A.; Gong, S. Multifunctional Stable and pH-Responsive Polymer Vesicles Formed by Heterofunctional Triblock Copolymer for Targeted Anticancer Drug Delivery and Ultrasensitive MR Imaging. *ACS Nano* **2010**, *4*, 6805−6817.
(48) Hickey, R. J.; Meng, X.; Zhang, P.; Park, S. Low-Dimensional Nanoparticle Clustering in Polymer Micelles and Their Transverse Relaxivity Rates. *ACS Nano* **2013**, *7*, 5824−5833.
(49) Pöselt, E.; Kloust, H.; Tromsdorf, U.; Janschel, M.; Hahn, C.; Maßlo, C.; Weller, H. Relaxivity Optimization of a PEGylated Iron-Oxide-Based Negative Magnetic Resonance Contrast Agent for T_2-Weighted Spin-Echo Imaging. *ACS Nano* **2012**, *6*, 1619−1624.
(50) Zhou, Z.; Tian, R.; Wang, Z.; Yang, Z.; Liu, Y.; Liu, G.; Wang, R.; Gao, J.; Song, J.; Nie, L.; Chen, X. Artificial Local Magnetic Field Inhomogeneity Enhances T_2 Relaxivity. *Nat. Commun.* **2017**, *8*, No. 15468.
(51) Kato, Y.; Ozawa, S.; Miyamoto, C.; Maehata, Y.; Suzuki, A.; Maeda, T.; Baba, Y. Acidic Extracellular Microenvironment and Cancer. *Cancer Cell Int.* **2013**, *13*, No. 89.
(52) Zhang, G.; Li, X.; Liao, Q.; Liu, Y.; Xi, K.; Huang, W.; Jia, X. Water-Dispersible PEG-Curcumin/Amine-Functionalized Covalent Organic Framework Nanocomposites as Smart Carriers for *In Vivo* Drug Delivery. *Nat. Commun.* **2018**, *9*, No. 2785.
(53) Lv, R.; Gai, S.; Dai, Y.; Niu, N.; He, F.; Yang, P. Highly Uniform Hollow GdF_3 Spheres: Controllable Synthesis, Tuned Luminescence, and Drug-Release Properties. *ACS Appl. Mater. Interfaces* **2013**, *5*, 10806−10818.

DOI: 10.1021/acs.chemmater.9b00028
Chem. Mater. 2019, 31, 3201−3210